Materials Today Physics 21 (2021) 100477

Contents lists available at ScienceDirect

Materials Today Physics

journal homepage: https://www.journals.elsevier.com/materials-today-physics

Inverse thermal design of nanoporous thin films for thermal cloaking

Yue Xiao, Qiyu Chen, Qing Hao*

Department of Aerospace and Mechanical Engineering, University of Arizona, Tucson, AZ, 85721, USA

ARTICLE INFO

Article history:
Received 12 May 2021
Received in revised form
19 June 2021
Accepted 30 June 2021
Available online 5 July 2021

Keywords:
Thermal cloak
Nanoporous
Inverse thermal design
Thermal camouflage
Thin film

ABSTRACT

In recent years, nanoporous thin films are widely studied as an effective way to improve the thermoelectric performance or manipulate the thermal transport within thin-film-based devices. In practice, nanoporous patterns can effectively cut off the heat flow and thus guide the thermal transport along the desired direction. However, a better design of these thermal devices is not addressed, such as thermal cloaking as the thermal counterpart for optical invisibility cloaks. In existing designs based on the Fourier's law, composite materials with varied structures are often introduced to achieve the required location-dependent thermal conductivities to distort the heat flux. At the micro-to nano-scale, such designs are difficult to be implemented and factors such as the interfacial thermal resistance must be further considered. In this work, inverse thermal designs of a nanoporous thin film are used to achieve the two-dimensional thermal cloaking, without introducing any other variation of the composition or material to tune the local thermal conductivity. This simple approach can be widely used for thin-film-based devices to protect heat-sensitive regions or function as thermal camouflaging devices. The proposed nanoporous structures can also be used to tune the local properties of a thin film for general applications, such as graded thermoelectric materials.

1. Introduction

In the last two decades, metamaterials to control the propagation of electromagnetic waves have received enormous attention [1–3]. Based on the analogy between electromagnetism and thermodynamics, thermal metamaterials for heat flux manipulation have also been developed [4–7]. One widely studied topic is thermal cloaking to protect a heat-sensing region or enable thermal sensors without disturbing the measured temperature field. Here the conventional Fourier's law for diffusive phonon transport is employed for thermal metamaterials, while photonic metamaterials assume wave effects. In a general design, a cloaking shell is added to distort the heat flux and shield the spherical or cylindrical inclusion from the background medium with a thermal conductivity k_b (Fig. 1). An additional shell, with a low thermal conductivity k_0, may be further added to thermally insulate the inclusion from the outer shell (Fig. 1b). The thermal design of the cloaking shell can be based on the mathematical analysis of coordinate transformation that compresses the region $r < R_2$ into a shell region $R_1 < r < R_2$ [2]. An anisotropic and graded thermal conductivity is required inside the shell. Guenneau et al. further extended the derivation to transient cases by taking into account the spatial distribution of the effective heat capacity [8]. To approximate the continuously graded thermal conductivity in experiments, the cylindrical or spherical cloaking shell is discretized into many sublayers along the radial direction, with carefully designed composite structures within each sublayer to yield the desired thermal properties. For two-dimensional (2D) thermal cloaking, Schittny et al. [9] first demonstrated 10 concentric porous Cu rings filled with polydimethylsiloxane to achieve the anisotropic and graded thermal conductivity k given by Guenneau et al. [8]. Ma et al. [10] constructed a similar work and five types of thin ingredient sheets within seven sublayers were used to adjust the local thermal properties, where noteworthy transient cloaking was achieved by further addressing the heat capacity within each sublayer. In theory, Li et al. proposed a graded nanoparticle-inserted spherical shell to achieve three-dimensional (3D) thermal cloaking [11], where a constant tangential-direction or azimuthal-component thermal conductivity k_φ and a graded radial-direction thermal conductivity k_r are used for the cloaking shells.

As a simplification of the coordinate-transformation design, Narayana et al. [12] suggested that $k_r/k_b = k_b/k_\varphi = C$ can be used for a cylindrical cloak, where k_r and k_φ represents the thermal conductivity along the radial and tangential directions,

* Corresponding author.
E-mail address: qinghao@email.arizona.edu (Q. Hao).

https://doi.org/10.1016/j.mtphys.2021.100477
2542-5293/

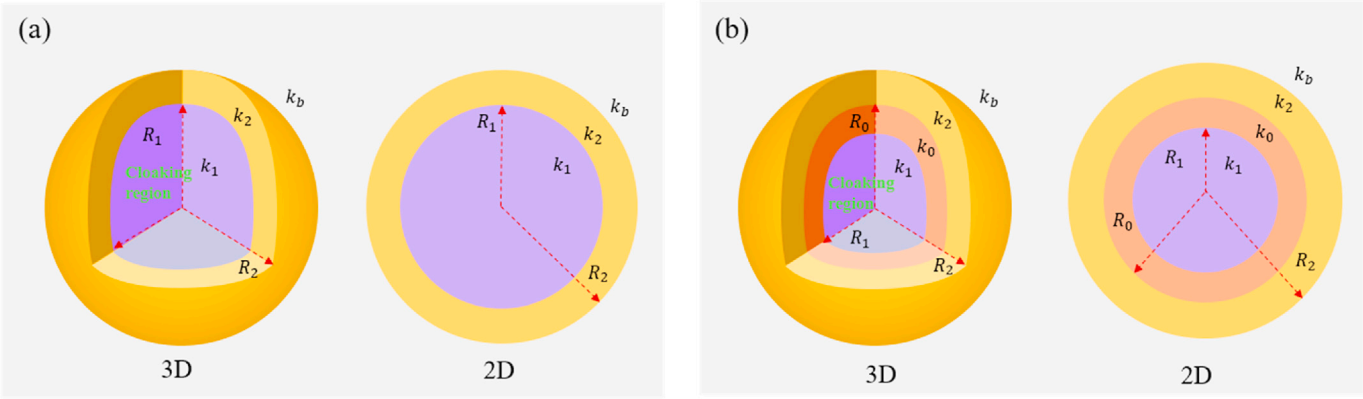

Fig. 1. Concept of thermal cloaking. (a) Schematic illustration of the 3D and 2D thermal cloaks, with the background medium as Region b ($r > R_2$), cloaking shell as Region 2 ($R_1 < r < R_2$), and shielded inclusion as Region 1 ($r < R_1$). (b) In some designs, the inclusion part is disconnected from the cloaking shell. In some cases, an extra thermal insulation shell with a very low thermal conductivity, as additional Region 0 for $R_1 < r < R_0$, is inserted between the two.

respectively. Here the constant C should satisfy $0 < C < ln(R_1/R_2)/[ln(R_1/R_2) - 1] < 1$. More discussions were given by Han et al. [13]. In this case, a smaller C indicates better cloaking performance, i.e., minimized thermal energy goes into the protected inclusion. Narayana et al. used 40 alternating layers of alternating concentric cylinders of latex rubber and a silicone elastomer to construct the anisotropic but homogeneous shell region under a steady homogeneous heat flux. Similar studies were also carried out by Dede et al. [14] using glass-epoxy FR-4 printed circuit board.

Even with the simplification by Narayana et al. [12], the above-mentioned composite structures are still challenging to be fabricated and the effective thermal conductivity cannot be exactly controlled. As a simpler method, the scattering cancellation approach is employed to achieve thermal cloaking with a zero scattering cross-section [15]. The advantage lies in that homogeneous materials can be used for a cloaking device to minimize the difficulty in manufacturing. As one breakthrough, Han et al. [16] experimentally demonstrated a homogeneous shell as a shielding device, which established the design methodology to create manufacturable 2D thermal cloaking devices. Xu et al. [17] demonstrated thermal cloak shielding of an air bubble in a bulk metal with a shell made of a thin layer of homogeneous and isotropic material. In a separated study, constant but different k_r and tangential-direction k_φ within the shell were suggested by Chen et al. [18]. Other thermal conductivity distributions are suggested by Farhat et al. [19].

Instead of using analytically derived thermal conductivities, a thermal cloak or a thermal-electrical bifunctional cloak was inversely designed with topology optimization [20,21]. A reverse thermal cloak design method was also proposed by Guo et al. as the density-based topology optimization [22]. In addition, the multi-scale inverse design of thermal composite structures for cloaking can also be found [23].

At the micro-to nano-scale, adding a cloaking shell around the protected region is not feasible due to the uncontrollable interfacial thermal resistance R_K between different material regions [24]. For 3D particle-in-a-host composites, the importance of R_K can be justified by the dramatically increased dimensionless $R_K k_b / d$ in the effective medium formulation, with d as the diameter of a spherical inclusion [25–28]. When composites are employed to achieve the designed thermal conductivity within the shell, the impact of the often unknown R_K can be significant [11]. Even for an isotropic and homogeneous shell suggested by the scattering cancellation approach, the R_K at the shell-medium interface can also be critical at small length scales. The critical R_K issue has been addressed by a recent study [29]. For thin films, modifications of the local thermal properties with the composite approach are not practical. On the other side, no good control for the obtained thermal conductivity is available for more advanced techniques such as local amorphization induced by ion implantation [30–33] and chemical functionalization [34].

In this work, nanoporous patterns [35–38] are proposed as a general approach to modify the local in-plane thermal conductivity for thermal cloaking within a thin film, with extensions to atomic-thick materials [39]. Despite some divergence between earlier measurements and theoretical predictions based on the phonon Boltzmann transport equation (BTE) [24,40,41], good agreements can now be obtained by improving the measurement techniques for various porous thin films [38,42–46]. This enables inverse thermal designs [47] to determine the nanoporous pattern for the desired thermal conductivities. In existing studies, nanoporous thin films have been proposed for heat guiding, emitters for directional heat rays, shielding, and thermal concentration [48,49]. However, the thermal design to achieve the exact temperature distribution such as 2D thermal cloaking is not addressed and is systemically studied here.

2. Inverse thermal design of 2D nanoporous patterns

Instead of wave effects for some phononic devices [50,51], particle-like phonons are considered here because existing studies suggest negligible wave effects in nanoporous Si thin films above ~10 K [52–54]. For lightly doped or undoped samples, the electronic part of the thermal conductivity can be neglected so that the overall thermal conductivity is mainly contributed by phonons. Assuming classical phonon size effects to decrease the effective phonon mean free paths (MFPs) and thus the lattice thermal conductivity, an inverse thermal design is used here to find the nanoporous pattern to achieve the targeted thermal conductivity. The porous pattern is first estimated with an analytical model. Phonon Monte Carlo (MC) simulations are then used to refine the geometry to achieve the exact thermal conductivity. The performance of the porous pattern is finally evaluated with phonon MC simulations for the obtained temperature profiles.

2.1. Homogeneous thermal conductivity for a 2D cloaking shell

For static 2D thermal cloaking, Han et al. [16] suggested a homogeneous and isotropic thermal conductivity within the shell

Table 1
Thermal conductivity distributions suggested in the literature. Cylindrical cloak: (r, φ, z); Spherical cloak: (r, θ, ϕ), $R_1 < r < R_2$. Transient thermal cloaking has further requirements for the product of the density ρ and specific heat c, e.g., works by Guenneau et al. [8], Zhang et al. [56], and Farhart et al. [57]. It should be noted that Xu et al. [17] is a special case with $k_1 = 0$ in the static-regime solution given by Farhart et al. [57].

Article	Thermal conductivity distribution	Method
Guenneau et al. [8] 2D	$k_r = \frac{r-R_1}{r}k_b,\ k_\varphi = \frac{r}{r-R_1}k_b$ $k_r = \left(\frac{R_2}{R_2-R_1}\right)^2\left(\frac{r-R_1}{r}\right)^2 k_b,\ k_\varphi = \left(\frac{R_2}{R_2-R_1}\right)^2 k_b$	Coordinate Transformation Method
Zhang et al. [56] 3D	$k_r = \frac{r-R_1}{r}k_b,\ k_\varphi = \frac{r}{r-R_1}k_b, k_z = \left(\frac{R_2}{R_2-R_1}\right)^2\frac{r-R_1}{r}k_b$ (cylindrical cloak) $k_r = \frac{R_2}{R_2-R_1}\frac{(r-R_1)^2}{r}k_b, k_\theta = \frac{R_2}{R_2-R_1}k_b, k_\phi = \frac{R_2}{R_2-R_1}k_b$ (spherical cloak)	
Narayana et al. [12] 2D	$\frac{k_r}{k_b} = \frac{k_b}{k_\varphi} = C, 0 < C < \frac{ln(R_1/R_2)}{ln(R_1/R_2)-1} < 1$	
Farhart et al. [57] 3D	$\frac{(k_b-k_2)(k_1+2k_2)}{(k_1-k_2)(k_b+2k_2)} = \gamma^3, \gamma = R_1/R_2$ (time-harmonic regime) $k_2 = \frac{-[(k_b-2k_1)\gamma^3+(2k_b-k_1)] + \sqrt{[(k_b-2k_1)\gamma^3+(2k_b-k_1)]^2+8k_bk_1(\gamma^3-1)^2}}{4(\gamma^3-1)}$ (static regime)	Scattering Cancellation Method
Han et al. [16] 2D	$k_2 = \frac{{R_2}^2+{R_0}^2}{{R_2}^2-{R_0}^2}k_b,\ k_0 = 0$ in Fig. 1b	
Xu et al. [17] 3D	$k_2 = \frac{2{R_2}^3+{R_0}^3}{2({R_2}^3-{R_0}^3)}k_b,\ k_0 = 0$ in Fig. 1b	

region, given as

$$k_2 = k_r = k_\varphi = \frac{R_2^2+R_0^2}{R_2^2-R_0^2}k_b > k_b, \tag{1}$$

which also assumed perfect thermal insulation between the shell and the protected cylindrical inclusion. In their work, an inner insulation shell made of ultra-low-k expanded polystyrene was added to block the thermal transport from the outer shell to the inclusion. For 2D films, such insulation can be easily achieved by removing an annulus region between the cylindrical inclusion and the outer shell region [9] or only leave narrow neck connections between the two regions [55]. To achieve the desired thermal conductivity distribution, the thin film should be patterned with nanoporosity to decrease k_b, whereas $k_r = k_\varphi$ can be maintained as the initial in-plane k of a solid thin film. Homogeneous and isotropic thermal conductivity for the cloaking region is also proposed by Farhat et al. [19] using the scattering cancellation technique. Above two isotropic thermal conductivities can be used for the design of the nanoporous films. Table 1 lists existing models for their proposed k values. Two methods are used to derive the required k distribution for 2D and 3D thermal cloaks, i.e., the coordinate transformation method and the scattering cancellation method. Here the coordinate transformation method often requires thermally anisotropic shells, which can be more difficult to be achieved in experiments. For the transient thermal cloaking, the product of the density ρ and specific heat c should also be matched [8,56,57]. More discussions are given in Section 3.3.

2.2. Analytical models to compute the lattice thermal conductivity

Fig. 2 displays two typical nanoporous patterns to tune the thermal properties, namely periodic circular pores and nanoslots. Aligned nanopores yield isotropic in-plane thermal conductivity, whereas nanoslot patterns result in an anisotropic in-plane thermal conductivity.

2.2.1. Aligned or staggered circular/square nanopores

In existing studies, classical phonon size effects are considered for nanoporous films above 300 K [36]. In general, the in-plane thermal conductivity k_L is given as [47,55].

$$k_L = \frac{F(\varphi)}{3}\sum_{i=1}^{3}\int_0^{\omega_{max,i}} c_p(\omega)v_{g,i}(\omega)\Lambda_{eff,i}(\omega)d\omega, \tag{2}$$

in which $c_p(\omega)$ and $v_{g,i}(\omega)$ are the differential volumetric phonon specific heat and phonon group velocity for the branch i and angular frequency ω, respectively. The correction factor $F(\varphi)$ accounts for the heat transfer reduction due to the porosity φ. In general, $F(\varphi)$ can be determined by the Fourier's law analysis, e.g., as the thermal conductance ratio between a porous film and its nonporous counterpart [58,59]. For films with aligned nanopores, the Hashin-Shtrikman factor [60] is found to be more accurate, given as

$$F(\varphi) = \frac{1-\varphi}{1+\varphi}. \tag{3}$$

To compute the effective phonon MFP Λ_{eff} in Eq. (2), the in-plane phonon MFP within a thin film (Λ_{Film}) is first calculated based on the bulk phonon MFP Λ_{Bulk} [61]:

$$\frac{\Lambda_{Film}}{\Lambda_{Bulk}} = 1 - \frac{3[1-P(\lambda)]\Lambda_{Bulk}}{2h}\int_0^1 \left(x-x^3\right)\frac{1-\exp\left(-\frac{h}{\Lambda_{Bulk}x}\right)}{1-P_1(\lambda)\exp\left(-\frac{h}{\Lambda_{Bulk}x}\right)}dx, \tag{4}$$

where $P(\lambda)$ is the specularity of film-surface phonon reflection for a film with its thickness h. Here λ is the phonon wavelength. Above 300 K, the surface roughness of films can be much larger than the ~1 nm phonon wavelength so that diffusive phonon reflection is dominant, i.e., $P(\lambda) \approx 0$ [61]. Using Λ_{Film}, $\Lambda_{eff} = (1/\Lambda_{Film} + 1/L_{eff})^{-1}$ can obtained using the Matthiessen's rule. Here L_{eff} is the characteristic length of a 2D nanoporous thin film, i.e., a thin film with specular phonon reflection on its top and bottom surfaces. This L_{eff} is unchanged for films with different thicknesses and varied phonon specularity at the top/bottom film surfaces. These additional factors are considered in Eq. (4) already.

Different L_{eff} expressions have been suggested in the literature

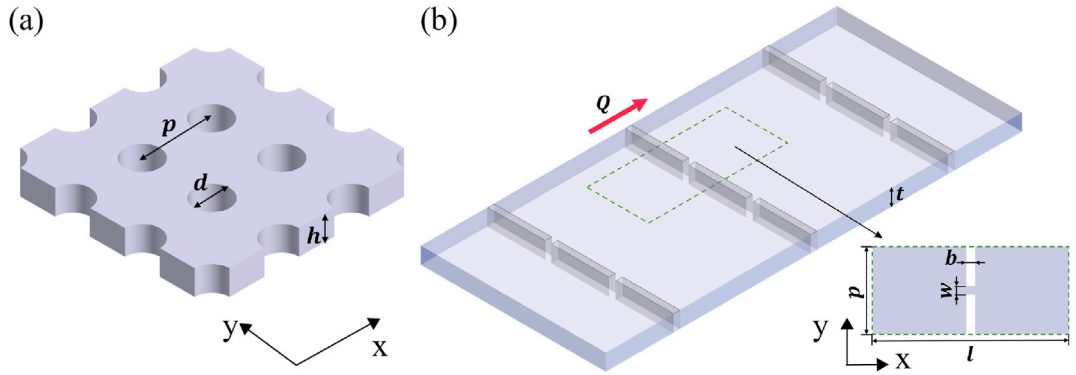

Fig. 2. Two typical nanoporous patterns to tune the thermal properties. (a) A film with periodic circular pores with pitch p, pore diameter d and film thickness h. (b) A film with periodic nanoslots. The inset figure shows the dimensions for one single period.

[59,62–65]. One widely used L_{eff} is the neck width between adjacent nanopores [62,63]. At the ballistic limit, the geometric mean beam length (MBL) for optically thin media in radiation [59,66] provides identical results as that extracted from MC ray tracing (MCRT) [67], in which the phonon scattering within the structure is tracked to statistically yield the L_{eff} value. Here the general form of MBL is $MBL = 4V_{solid}/A$, where V_{solid} is the solid volume of a period and A is the pore surface area. Such a general expression is applicable to thin films with arbitrary patterns, including both square and circular pores. Particularly for patterns with a pitch p and pore diameter d, the MBL for two typical porous patterns is given as [38,68]

$$MBL = \begin{cases} \dfrac{4p^2 - \pi d^2}{\pi d} \ (square\ lattice) \\ \dfrac{2\sqrt{3}p^2 - \pi d^2}{\pi d} \ (hexagonal\ lattice) \end{cases}. \tag{5}$$

The use of the MBL as L_{eff} can be further extended to 3D nanoporous bulk materials [66] and atomic thick materials with aligned nanopores [39]. Particularly for nanoporous 2D materials with a reduced degree of freedom for phonon movement, the MBL is changed to a different expression [36]

$$MBL = \frac{\pi S_{Solid}}{P}. \tag{6}$$

For nanoporous 2D materials, S_{solid} corresponds to the solid area of a period and P is the pore perimeter. The MBL expression in Eq. (6) is close to $L_{eff} \approx 3.4S_{Solid}/P$ obtained by fitting the MCRT results of a 2D porous pattern [59]. When the pore shape is changed, the MBL is still valid because it captures the surface area to scatter phonons per unit solid volume. In practice, the MBL can be viewed as the upper bound for L_{eff}, whereas the neck width is the lower bound.

2.2.2. Aligned or offset nanoslots

Other than periodic circular/square pores, nanoslots can also be used to tailor the thermal conductivity (Fig. 2b). With a narrow neck width w between nanoslots, phonons should travel ballistically through the neck region. Such ballistic phonon transport leads to strongly suppressed thermal transport and an associated ballistic thermal resistance [55,69]. One advantage of using nanoslots lies in that an accurate L_{eff} expression is available [35,55]. When the neck depth b is very small, L_{eff} to compute k_x is given as

$$L_{eff} \approx \frac{w}{p-w}\frac{3l}{4H_w}, \tag{7}$$

in which the correction factor H_w plays the same role as $F(\varphi)$ in Eq. (2) and is evaluated along the direction perpendicular to the nanoslots. When the b value is large, an additional thermal resistance for the neck region, as a rectangular nanowire with its length b, should be added to the overall thermal resistance of the structure. For Si thin films with periodic nanoslots, this correction is usually negligible for b<5 nm [35]. Equation (7) is generally accurate when p/w and p/l are not too large to avoid "thermally dead" regions contributing little to the heat conduction [70]. Experimentally, the "thermally dead" region is observed at $p/w = 6.9$ for a Si nanoladder [70]. In calculations, the divergence between k_L predicted using L_{eff} from Eq. (7) and phonon MC simulations increases to 14% at $p/w = 10$ for selected nanoslot patterns [35], indicating the increased thermally dead region at larger p/w ratios. When b is not negligible, the thermal resistance of the neck region as a rectangular nanowire should be added and accurate k_x predictions can still be obtained. Along the y direction in Fig. 2b, bulk-like thermal conductivity can be maintained when b/l is small and l is still large compared with majority phonon MFPs within a solid thin film. A high thermal anisotropy can thus be obtained with such nanoslot patterns.

2.3. Phonon MC simulations for thermal conductivity calculations

Frequency-dependent phonon MC simulations are carried out to obtain the temperature distribution within nanopore-modified thin films [71]. For the estimated nanoporous patterns of the background medium, the effective thermal conductivity is also cross-checked with the phonon MC simulations, with minor adjustments on the pitch of the nanoporous structures to achieve the exact thermal conductivity. In phonon MC simulations, the transport and scattering of individual phonons inside the computational domain is tracked. For periodic structures, a boundary condition, assuming a periodic heat flux with constant virtual wall temperatures, can be imposed to the computational domain to simulate a single period of the structure [71]. Arbitrary nanostructure shapes can be defined in phonon MC simulations with specified phonon scattering at nanostructured boundaries or interfaces. To obtain the temperature profile, the computational domain is divided into many rectangular subcells as spatial bins to count the local temperature based on the phonon energy density within each subcell. Rectangular nanostructure shapes are assumed in most studies to be consistent with rectangular subcells. More complicated shapes,

such as circular pores, may also be handled when the solid volume of subcells on the pore edge can be accurately evaluated for the calculations of the subcell temperature [72]. When the simulation converges, the lattice thermal conductivity can be obtained using the heat flow extracted from the phonon tracking and the temperature difference across the computational domain. Using the phonon MC simulations, the phonon BTE can be solved statistically. In existing studies, a nanoscale computational domain is usually used for thermal devices using nanoporous thin films [48,49]. However, a micro-scale computational domain is required for the simulations of 2D thermal cloaking, which is achieved with the computationally efficient deviational phonon MC technique developed by Péraud and Hadjiconstantinou [73]. In contrast with conventional phonon MC simulations tracking all phonons [71], this new technique only focuses on phonons corresponding to the deviation of the phonon distribution function f from the equilibrium f_0 (i.e., Bose-Einstein distribution) at a reference temperature. This enables phonon MC simulations for the proposed microsized thin films. Detailed discussion on the adopted phonon MC simulations is in the Supplementary Material, and more introductions on phonon MC simulations can be found elsewhere [36].

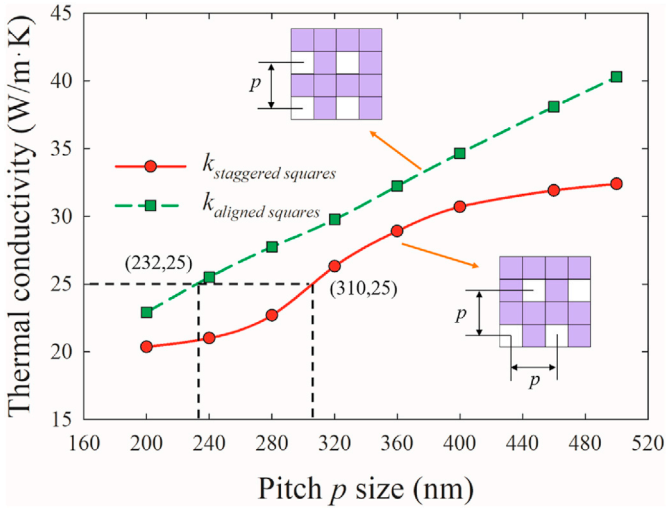

Fig. 3. Pitch-dependent in-plane lattice thermal conductivity of a film with aligned and staggered square pores. Porosity φ is fixed at 25%. Insets: illustration of the aligned and staggered square pores.

3. Results and discussion

3.1. Thermal cloaking with thin films modified by square nanopores

Among all models in Table 1, the simple design for 2D thermal cloaking is proposed by Han et al. [16]. Using a solid film as the cloaking region, the background k_b is thus

$$k_b = k_2 \frac{R_2^2 - R_0^2}{R_2^2 + R_0^2}, \tag{8}$$

where a smaller k_b can be achieved by uniformly distributed pores in regions outside the cloaking shell.

Although circular pores are usually fabricated in real nanoporous films, the treatment of circular pores is very complicated and square pores are often used to simplify the simulations, without changing the fundamental physics of classical phonon size effects due to diffusive pore-edge phonon scattering. Using a 220-nm-thick solid Si thin film with an in-plane k = 65 W/m·K at 300 K, k_b = 25 W/m·K is required for R_2/R_0 = 1.5 according to Eq. (8). When the electronic part of the thermal conductivity is neglected, these thermal conductivities can be mainly attributed to the lattice contribution. To achieve this k_b, the analytical model in Section 2.2.1 can be used to generate an initial estimation, and phonon MC simulations are then used to refine the results. Using phonon MC simulations, Fig. 3 shows the in-plane lattice thermal conductivity of 220-nm-thick Si films with aligned and staggered square pores. The porosity is fixed at φ = 25%, and the pitch p (Fig. 3 insets) varies from 200 nm to 500 nm. The employed bulk phonon MFP Λ_{Bulk} in phonon MC simulations is from Wang et al. [74] by fitting the temperature-dependent lattice thermal conductivity of bulk Si. To achieve the targeted k_b = 25 W/m·K, the pitch size should be p = 310 nm and p = 232 nm for staggered and aligned pores, respectively. When the MBL is used, the estimated p value is 184 nm for both aligned and staggered patterns. If a different R_2/R_0 ratio is employed, the corresponding pitch size can also be determined from Fig. 3.

The 2D thermal cloak design using the estimated k_b is validated by phonon MC simulations, from which the temperature profile is extracted. For the same 220-nm-thick Si film, the staggered square pore pattern is adopted in the design, with p = 310 nm, R_2 = 9.3 μm, and R_2/R_0 = 1.5. Isothermal walls are assigned as the left and right boundaries of the simulated structure, whereas the top and bottom boundaries are adiabatic. The complete computational domain has a size of 27.9 μm × 27.9 μm × 220 nm. A single circular pore with its radius R_0 is placed in the center to represent the thermally insulated region. It should be noted that the background thermal conductivity modification is based on nanopores with sizes much smaller than R_2. The overall temperature distribution in the porous region is close to a homogeneous material although nanoporosity can distort local heat fluxes at the nanoscale. The simulated temperature profile is shown in Fig. 4a, with a hot left end and a cold right end. The black dots in the background are the staggered square pores. In nanofabrication, a similar hexagonal porous pattern can be defined using a self-assembled monolayer of nanospheres or block co-polymer for mass production [36,40,43]. Ion implantation [30–33] can also be used to achieve the reduced k_b but the obtained thermal conductivity cannot be easily controlled. In comparison, the temperature profile of the 2D thermal cloak using different homogeneous solid materials for the background k_b and cloaking-region k_2 is also extracted using Fourier's law analysis via COMSOL Multiphysics® software package (Fig. 4b) that adopts the finite element method. For the Fourier's law analysis in COMSOL, the computational domain size, boundary conditions, and the core-shell dimension are the same as those in the phonon MC simulations. Here 23,664 nodes are used in the COMSOL simulations, and an increased number of nodes does not affect the result. The relationship between k_b and k_2 satisfies Eq. (8) to achieve the ideal design of a thermal cloak, i.e., k_b = 25 W/m·K and k_2 = 65 W/m·K.

3.2. Thermal cloaking effectiveness

To evaluate the thermal cloak effectiveness, Petiteau et al. [75] and Hu et al. [76] proposed quantitative analysis methods with a standard deviation to evaluate the thermal cloaking effectiveness. In addition, Guo et al. [22] proposed a simpler method to assess the cloak effectiveness where the peripherical temperature at $r = R_2$ of a thermal cloak design were extracted and compared to that of the solid film. This quantitative analysis is adopted here, using the normalized temperature defined as $T^* = (T - T_{hot})/(T_{cold} - T_{hot})$, where T_{hot} and T_{cold} are the temperatures of the left and right sides, respectively. The results are shown in Fig. 5. The line with symbols

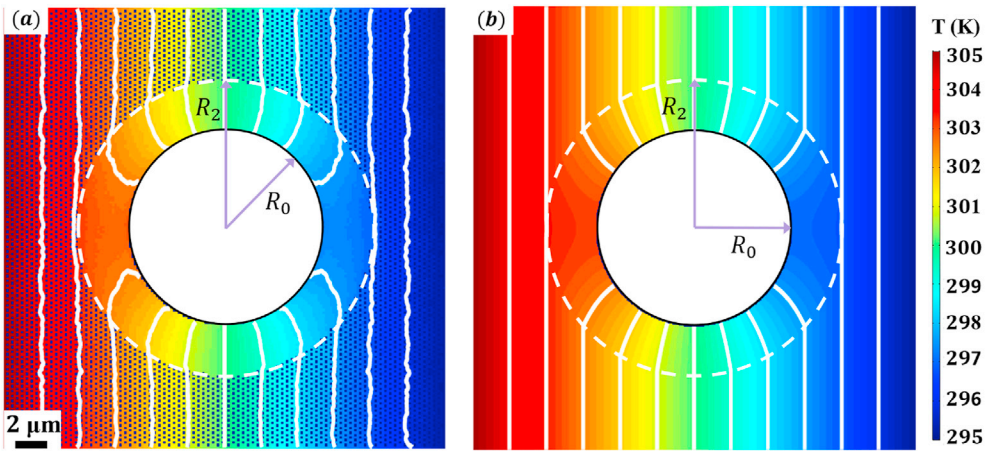

Fig. 4. (a) Temperature profile extracted from phonon MC simulations of the designed 2D thermal cloak using staggered square nanopores to modify k_b. (b) Fourier's law analysis of the designed 2D thermal cloak using two homogeneous solid materials. White lines are the isothermal lines for representative temperatures.

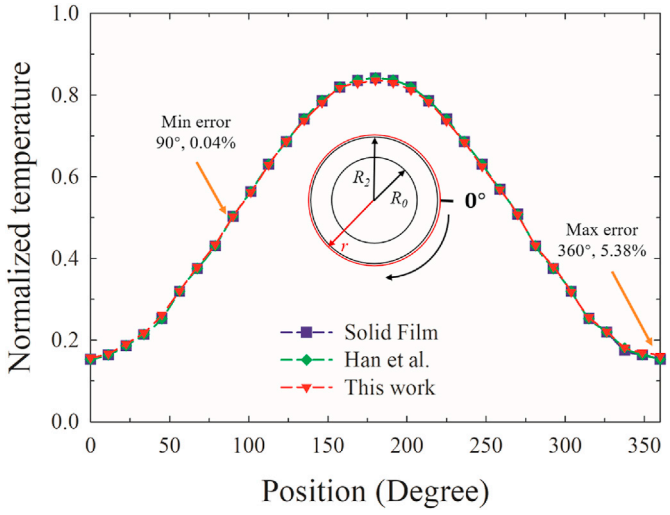

Fig. 5. Comparison between the temperature profiles at $r = 9.61\mu m$ for different designs and a reference solid thin film.

is the temperature distribution at $r = 9.61\mu m$, representing the temperature changes around the edge of the thermal cloak. The selection of a radius slightly larger than R_2 is mainly due to the less accurately defined boundary between the solid shell and the porous background medium. The line with triangle down symbols is the temperature distribution of our design. The lines with diamond symbols and square symbols are the temperature distributions of the design by Han et al. [16] and a reference solid film, respectively. The normalized temperature values at selected points on the solid film exactly match that computed by the model given by Han et al. [16]. The maximum error is 5.38% between the thermal cloaking design in this work and the reference solid film. In general, our design and the design by Han et al. agree very well with the reference solid film.

3.3. Nanoslot patterns for anisotropic **k** within the cloaking shell

One thermal design for a 2D cloaking shell, as proposed by Narayana et al. [12], assumes constant but anisotropic thermal conductivities along two major directions, i.e.,

$$\frac{k_r}{k_b} = \frac{k_b}{k_\varphi} = C, \tag{9a}$$

and

$$0 < C < \frac{ln(R_1/R_2)}{ln(R_1/R_2) - 1} < 1 \tag{9b}$$

A smaller C value is preferred for better cloaking performance. This design requires $k_r < k_b < k_\varphi$. In this case, nanoslot patterns can be introduced for the shell region to achieve a highly anisotropic thermal conductivity, whereas the background medium can be modified by uniformly distributed nanoporous to lower k_b (Fig. 6). For the cloaking shell, periodic nanoslots can be widely used to achieve a high thermal anisotropy [35,37]. The thermal conductivity k_x perpendicular to the nanoslots (Fig. 2b) can be largely reduced from the bulk value, which can be used to achieve the k_r value in the model by Narayana et al. [12]. This k_r can be further reduced with offset nanoslots [37]. On the other hand, the thermal conductivity k_y along the nanoslot direction, functioning as k_φ in Fig. 6, can be maintained as the bulk value when the nanoslot depth b is negligible and l is much larger than phonon MFPs.

The complicated structure geometry in Fig. 6 cannot be easily treated in phonon MC simulations that may require irregular subcells to fit the curved shapes. In addition, the algebra to compute the randomized phonon reflection by irregular pores can also be complicated. However, the inverse design procedure can still be demonstrated here. For nanoslot-patterned cloaking shell, frequency-dependent phonon MC simulations are utilized to determine the in-plane thermal conductivities of 2D Si thin films with aligned and offset nanoslots patterns. In a 2D thin film, specular phonon reflection is assumed for top and bottom film surfaces so that the film thickness does not affect the resulting in-plane thermal conductivities. When diffusive film-surface phonon scattering is considered, Λ_{Film} given by Eq. (4) can be simply used to replace Λ_{Bulk} and the rest of the computation is unchanged [47]. The x-directional thermal conductivities of 2D Si thin films with offset ($k_{x,offset}$) and aligned ($k_{x,aligned}$) nanoslots patterns are obtained from frequency-dependent phonon MC simulations. The neck width w of the nanoslots structure varies from 20 nm to 120 nm and the corresponding porosity changes from 30.6% to 16.7%. Other parameters are fixed as $l = 30$ nm, $p = 240$ nm, and $b = 10$ nm. In Fig. 7a, the y-directional thermal conductivity k_y is identical for both offset and aligned nanoslots patterns. To design

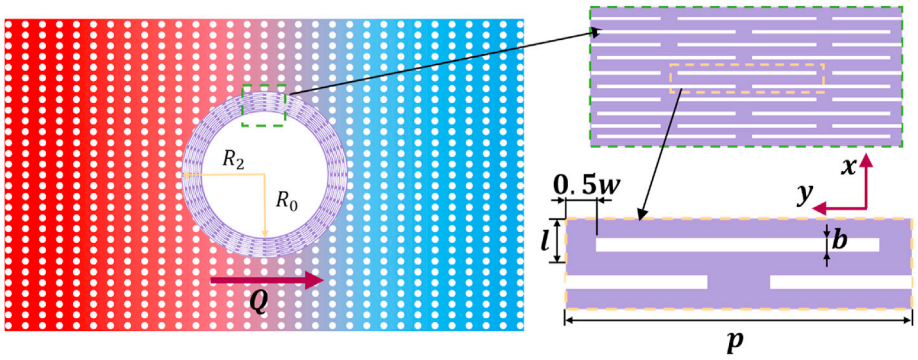

Fig. 6. Design of a nanoslot- and nanopore-patterned 2D thermal cloak.

the thermal cloak with $R_2/R_1 = R_2/R_0 = 1.5$, a condition similar to Sec. 3.1, is assumed in Eq. (9b). Assuming the targeted $k_b = 4.7$ W/m·K and the offset nanoslot geometry in Fig. 6, $C = 0.21$ can be selected so that $k_r = k_{x,offset} = 1$ W/m·K and $k_\varphi = k_y = 22$ W/m·K to satisfy Eq. (9). To achieve such k_r and k_φ, the design of the aligned/offset nanoslot patterns are predicted by the frequency-dependent phonon MC simulation as a function of neck width (Fig. 7). From Fig. 7, the offset nanoslot geometry, with neck width $w = 100$ nm, can be selected to determine the nanoslot patterns. For thin films with a thickness h, a two-step phonon MFP modification can be adopted to quickly determine the in-plane thermal conductivity and thus the proper nanoslot design [47].

In another model given by Guenneau et al. [8], a radius-dependent k_r but a constant k_φ are suggested:

$$k_r = \left(\frac{R_2}{R_2 - R_1}\right)^2 \left(\frac{r - R_1}{r}\right)^2 k_b, \tag{10a}$$

$$k_\varphi = \left(\frac{R_2}{R_2 - R_1}\right)^2 k_b. \tag{10b}$$

Such a graded k_r can be achieved by increasing the neck width w from zero at $r = R_1$ to pitch p (i.e., no nanoslots) at $r = R_2$. For transient thermal cloaking, ρ_{eff} and c_{eff} should be unchanged from the cloaking shell to the background region. This can be achieved in nanoporous structures, as the heat capacity is determined solely by the porosity at 300 K. Although phonon wave effects within a periodic pattern [24,36] may modify the phonon dispersion and thus the phonon specific heat, the diffusive phonon scattering by rough pore edges usually destroys the phonon phase coherence and thus wave effects. Above 77 K, bulk-like specific heat was measured on nanoporous Si films with ~100 nm pitches [42]. For nanoslot patterns, the neck region as a short rectangular nanowire may also have phonon dispersion variation from the bulk counterpart but the overall impact is small with a very small depth b. Based on the above discussions, the maintained $\rho_{eff} c_{eff}$ can be satisfied when the porosity is fixed across a thin film. The variation of the in-plane thermal conductivity can be achieved by changing the porous pattern for the alignment, size, and shape of nanopores.

3.4. Thermal camouflage

The studied thermal cloaking can be extended to thermal camouflage [77,78] as a perfect thermal illusion device. Two symmetric C-shaped regions, as three interconnected pores attached to the cloaking shell, are added to the 220-nm-thick Si films in Section 3.1 to demonstrate the thermal camouflaging effect. Using phonon MC simulations, Fig. 8a shows the thermal profile of such a thermal camouflaging device. These regions are the designed thermal illusion, while the thermal feature in the center region is concealed within the thermal cloak and becomes transparent.

The camouflage effect is validated in Fig. 9 by comparing the temperature profile outside the cloaking region to that of a homogeneous porous film with the same mimicked C-shape objects, as shown in Fig. 8b. The same evaluation method in Fig. 5 is employed. The normalized temperature profiles at selected points within Fig. 8a (green diamond) and Fig. 8b (red down triangle) are shown in Fig. 9, with <9.1% divergence in general. All temperature

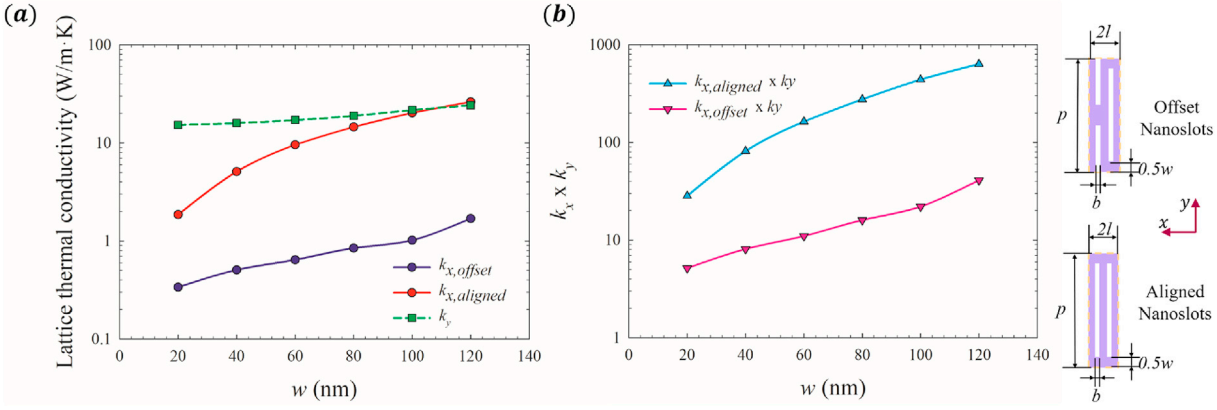

Fig. 7. (a) Representative k_x (i.e., k_r). and k_y (i.e., k_φ) values for 2D periodic nanoslots with w varying from 20 nm to 120 nm. Other geometry parameters are $l = 30$ nm, $p = 240$ nm, and $b = 10$ nm. Insets: illustration of the aligned and offset nanoslot patterns. (b) $k_x \times k_y$ as a function of w.

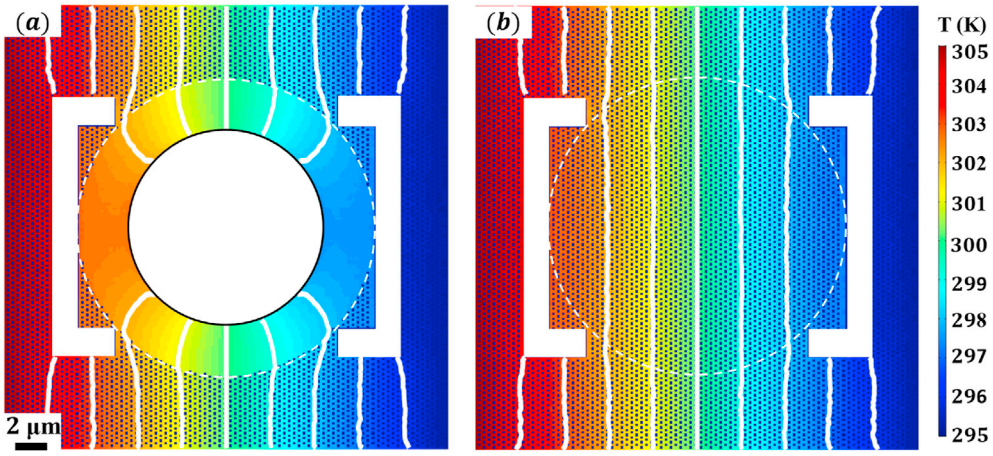

Fig. 8. (a) Temperature profile of a thermal camouflaging device to hide the thermal feature of the center region. (b) Temperature profile of a reference Si film. White lines are the isothermal lines for representative temperatures.

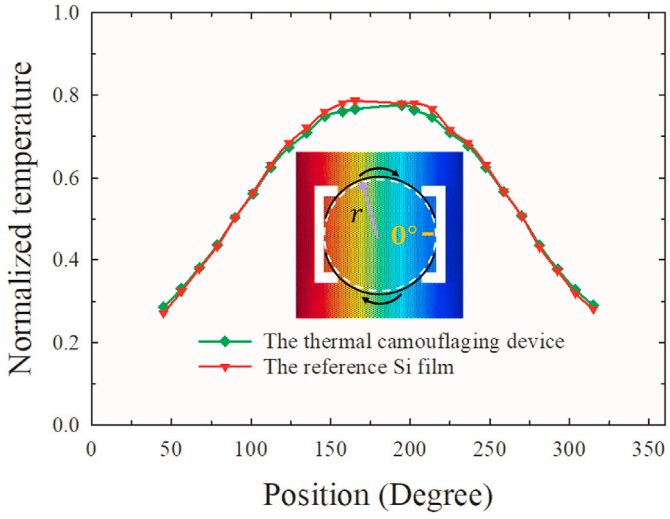

Fig. 9. Temperature comparison along the black solid line, $r = 9.61\mu m$, for a film with/without the thermal cloak. Two C-shaped regions are introduced as the thermal illusion.

points are extracted along the black solid line in Fig. 9, $r = 9.61\ \mu m$, outside the cloaking region (white dash line) in Fig. 8.

4. Conclusions

In this work, periodic square nanopores and rectangular nanoslots are proposed as an effective approach to locally tune the thermal conductivity and thermal anisotropy of thin films, and potentially atomic-thick materials. The thermal cloaking effectiveness [22] is computed and compared to theoretical predictions for the recommended continuous thermal conductivity distributions. This new approach enables 2D thermal cloaking for thin-film devices by eliminating the challenges in fabricating nanocomposites with well-controlled thermal properties. Based on the initial guess with the MBL as the characteristic length and further refinement with phonon MC simulations, inverse thermal designs are used to obtain the targeted thermal conductivity, which may be further improved with machine learning models [79,80]. A homogeneous and isotropic thermal conductivity, reduced from that for the solid counterpart, can be obtained in films with periodic circular/square nanopores. For anisotropic thermal conductivities, offset nanoslots with an extremely small depth and adjustable neck width between adjacent nanoslots can be used to achieve a high thermal anisotropy, while keeping the heat capacity very close to that for a solid film. Such a structure can be widely used for transient thermal cloaking as suggested by Guenneau et al. [8]. This work provides new directions for fabricating 2D thermal cloaking and other devices, such as thermal camouflage, concentration, and inversion [56,81]. For thermoelectric applications, the same nanoporous patterns have much less impact on the electrical properties because electrons usually have a much shorter MFP than phonons. In this case, well-designed nanoporous patterns can yield graded thermoelectric properties and better compatibility between the *n*- and *p*-type legs, resulting in optimized device performance [82,83].

Declaration of competing interest

The authors declare that they have no known competing financial interests or personal relationships that could have appeared to influence the work reported in this paper.

Acknowledgments

The authors thank the University of Arizona Research Computing High Performance Computing (HPC) and High Throughput Computing (HTC) for the allocation of computing time. This work is supported by the National Science Foundation [grant number CBET-1651840] for studies on MC simulations.

Credit author statement

Yue Xiao: Phonon Monte Carlo simulations, Writing some paragraphs; Qiyu Chen: Formal analysis, Plotting figures; Qing Hao: Conceptualization, Methodology, Writing.

Appendix A. Supplementary data

Supplementary data to this article can be found online at https://doi.org/10.1016/j.mtphys.2021.100477.

References

[1] J.B. Pendry, et al., Phys. Rev. Lett. 76 (25) (1996) 4773.
[2] J.B. Pendry, et al., Science 312 (5781) (2006) 1780–1782.
[3] U. Leonhardt, Science 312 (5781) (2006) 1777–1780.

[4] C.Z. Fan, et al., Appl. Phys. Lett. 92 (25) (2008): 251907.
[5] J.-P. Huang, Theoretical Thermotics - Transformation Thermotics and Extended Theories for Thermal Metamaterials, 1 ed., Springer Singapore, Singapore, 2020.
[6] T. Chen, et al., Appl. Phys. Lett. 93 (11) (2008) 114103.
[7] R. Hu, et al., Mater. Today 45 (2021) 120–141, https://doi.org/10.1016/j.mattod.2020.11.013.
[8] S. Guenneau, et al., Opt Express 20 (7) (2012) 8207–8218.
[9] R. Schittny, et al., Phys. Rev. Lett. 110 (19) (2013) 195901.
[10] Y. Ma, et al., NPG Asia Mater. 5 (11) (2013) e73-e73.
[11] J. Li, et al., J. Appl. Phys. 108 (7) (2010): 074504.
[12] S. Narayana, Y. Sato, Phys. Rev. Lett. 108 (21) (2012) 214303.
[13] T. Han, et al., Sci. Rep. 3 (2013) 1593.
[14] E.M. Dede, et al., Appl. Phys. Lett. 103 (6) (2013): 063501.
[15] A. Alù, N. Engheta, Phys. Rev. 72 (1) (2005): 016623.
[16] T. Han, et al., Phys. Rev. Lett. 112 (5) (2014): 054302.
[17] H. Xu, et al., Phys. Rev. Lett. 112 (5) (2014): 054301.
[18] T. Chen, et al., J. Appl. Phys. 117 (5) (2015): 054904.
[19] M. Farhat, et al., Sci. Rep. 5 (1) (2015) 9876.
[20] G. Fujii, et al., Appl. Phys. Lett. 112 (6) (2018): 061108.
[21] G. Fujii, Y. Akimoto, Appl. Phys. Lett. 115 (17) (2019) 174101.
[22] J. Guo, et al. 7, ES Energy & Environment, 2020, pp. 71–83.
[23] E.M. Dede, et al., Struct. Multidiscip. Optim. 49 (1) (2014) 59–68.
[24] D.G. Cahill, et al., Appl. Phys. Rev. 1 (1) (2014): 011305.
[25] Y. Xu, et al., Composites Communications 24 (2021) 100617.
[26] C.-W. Nan, et al., J. Appl. Phys. 81 (10) (1997) 6692–6699.
[27] D. Hasselman, L.F. Johnson, J. Compos. Mater. 21 (6) (1987) 508–515.
[28] Y. Benveniste, J. Appl. Phys. 61 (8) (1987) 2840–2843.
[29] X. Zheng, B. Li, Physical Review Applied 13 (2) (2020): 024071.
[30] Y. Xiao, et al., Materials Today Physics (2020) 100179.
[31] E.A. Scott, et al., Carbon 157 (2020) 97–105.
[32] Y. Zhao, et al., Nat. Commun. 8 (1) (2017) 1–8.
[33] Y. Liu, et al., Phys. Lett. 383 (19) (2019) 2296–2301.
[34] Z.-Q. Ye, B.-Y. Cao, Phys. Chem. Chem. Phys. 18 (48) (2016) 32952–32961.
[35] Q. Hao, Y. Xiao, Physical Review Applied 13 (6) (2020): 064020.
[36] Y. Xiao, et al., ES Materials & Manufacturing 5 (2019) 17.
[37] Y. Xiao, Q. Hao, Int. J. Heat Mass Tran. 170 (2021) 120944.
[38] D. Xu, et al., Front. Energy 12 (1) (2018) 127–136.
[39] Q.-Y. Li, et al., Engineered Science (2) (2020).
[40] J. Tang, et al., Nano Lett. 10 (10) (2010) 4279–4283.
[41] J.-K. Yu, et al., Nat. Nanotechnol. 5 (10) (2010) 718–721.
[42] Q. Hao, et al., Sci. Rep. 8 (1) (2018) 9056.
[43] J. Lim, et al., ACS Nano 10 (1) (2016) 124–132.
[44] M. Nomura, et al., Appl. Phys. Lett. 109 (17) (2016) 173104.
[45] M. Nomura, et al., Jpn. J. Appl. Phys. 57 (8) (2018): 080101.
[46] R. Anufriev, et al., Phys. Rev. B 101 (11) (2020) 115301.
[47] Q. Hao, et al., Int. J. Heat Mass Tran. 153 (2020) 119636.
[48] R. Anufriev, et al., Nat. Commun. (2017) **8**.
[49] R. Anufriev, M. Nomura, Materials Today Physics 15 (2020) 100272.
[50] M. Maldovan, Phys. Rev. Lett. 110 (2) (2013): 025902.
[51] M. Maldovan, Nat. Mater. 14 (7) (2015) 667.
[52] J. Lee, et al., Nat. Commun. 8 (2017) 14054.
[53] J. Maire, et al., Science advances 3 (8) (2017): e1700027.
[54] N. Zen, et al., Nat. Commun. 5 (2014) 3435.
[55] Q. Hao, et al., Materials Today Physics (2019) **10**.
[56] Y.M. Zhang, et al., AIP Adv. 5 (5) (2015).
[57] M. Farhat, et al., Sci. Rep. 5 (2015) 9876.
[58] A. Jain, et al., Phys. Rev. B 87 (19) (2013) 195301.
[59] Q. Hao, et al., J. Appl. Phys. 120 (6) (2016): 065101.
[60] Z. Hashin, S. Shtrikman, J. Appl. Phys. 33 (10) (1962) 3125–3131.
[61] G. Chen, Nanoscale Energy Transport and Conversion: A Parallel Treatment of Electrons, Molecules, Phonons, and Photons, Oxford University Press, New York, 2005.
[62] P.E. Hopkins, et al., Appl. Phys. Lett. 95 (16) (2009) 161902.
[63] P.E. Hopkins, et al., Appl. Phys. A 103 (3) (2011) 575–579.
[64] S. Alaie, et al., Nat. Commun. 6 (2015) 7228.
[65] C. Huang, et al., Phys. E Low-dimens. Syst. Nanostruct. 97 (2018) 277–281.
[66] Q. Hao, et al., Appl. Therm. Eng. 111 (2017) 1409–1416.
[67] D. Lacroix, et al., Phys. Rev. B 72 (6) (2005): 064305.
[68] Q. Hao, et al., J. Appl. Phys. 121 (9) (2017): 094308.
[69] B.-Y. Cao, et al., Carbon 96 (2016) 711–719.
[70] W. Park, et al., Nanoscale 10 (23) (2018) 11117–11122.
[71] Q. Hao, et al., J. Appl. Phys. 106 (11) (2009) 114321.
[72] Q. Hao, et al., Appl. Therm. Eng. 111 (2017) 1409–1416.
[73] J.-P.M. Péraud, N.G. Hadjiconstantinou, Phys. Rev. B 84 (20) (2011) 205331.
[74] Z. Wang, et al., Nano Lett. 11 (6) (2011) 2206–2213.
[75] D. Petiteau, et al., Sci. Rep. 4 (2014) 7386.
[76] R. Hu, et al., Chin. Phys. Lett. 33 (4) (2016): 044401.
[77] T. Han, et al., Adv. Mater. 26 (11) (2014) 1731–1734.
[78] T.-Z. Yang, et al., Appl. Phys. Lett. 109 (12) (2016) 121905.
[79] H. Wei, et al., Nanomater. Energy 71 (2020) 104619.
[80] H. Wei, et al., Int. J. Heat Mass Tran. 127 (2018) 908–916.
[81] I. Peralta, et al., Adv. Eng. Mater. 22 (2) (2020) 1901034.
[82] G.J. Snyder, T.S. Ursell, Phys. Rev. Lett. 91 (14) (2003) 148301.
[83] Z. Bian, A. Shakouri, Appl. Phys. Lett. 89 (21) (2006) 212101.